JPhys Materials

PAPER • OPEN ACCESS

Dirac materials under linear polarized light: quantum wave function time evolution and topological Berry phases as classical charged particles trajectories under electromagnetic fields

To cite this article: V G Ibarra-Sierra *et al* 2022 *J. Phys. Mater.* **5** 014002

View the article online for updates and enhancements.

You may also like

- Stacking and freestanding borophene for lithium-ion battery application
Wei Shao, Chuang Hou, Zenghui Wu et al.
- Optical properties of two-dimensional materials with tilted anisotropic Dirac cones: theoretical modeling with application to doped 8-*Pmmn* borophene
Vl A Margulis and E E Muryumin
- Probing borophene oxidation at the atomic scale
Xiaolong Liu, Matthew S Rahn, Qiyuan Ruan et al.

This content was downloaded from IP address 189.147.89.198 on 30/11/2023 at 23:16

IOP Publishing J. Phys. Mater. 5 (2022) 014002 https://doi.org/10.1088/2515-7639/ac5231

Journal of Physics: Materials

OPEN ACCESS

RECEIVED
27 November 2021

REVISED
26 January 2022

ACCEPTED FOR PUBLICATION
4 February 2022

PUBLISHED
22 February 2022

Original Content from this work may be used under the terms of the Creative Commons Attribution 4.0 licence.

Any further distribution of this work must maintain attribution to the author(s) and the title of the work, journal citation and DOI.

PAPER

Dirac materials under linear polarized light: quantum wave function time evolution and topological Berry phases as classical charged particles trajectories under electromagnetic fields

V G Ibarra-Sierra[1,2], J C Sandoval-Santana[1,3,*], A Kunold[1], Saúl A Herrera[4] and Gerardo G Naumis[4]

[1] Área de Física Teórica y Materia Condensada, Universidad Autónoma Metropolitana Azcapotzalco, Av. San Pablo 180, Col. Reynosa-Tamaulipas, 02200 Cuidad de México, México
[2] Facultad de Ciencias, Universidad Autónoma de Baja California, Apartado Postal 1880, 22800 Ensenada, Baja California, México
[3] Centro de Nanociencias y Nanotecnología, Universidad Nacional Autónoma de México, Apartado Postal 2681, 22800 Ensenada, Baja California, México
[4] Departamento de Sistemas Complejos, Instituto de Fisica, Universidad Nacional Autónoma de México, Apartado Postal 20-364, 01000 Ciudad de México, México
[*] Author to whom any correspondence should be addressed.

E-mail: jcss@ens.cnyn.unam.mx

Keywords: Dirac materials, topological phases, time driven systems, graphene, borophene

Abstract

The response of electrons under linearly polarized light in Dirac materials as borophene or graphene is analyzed in a continuous wave regime for an arbitrary intense field. Using a rotation and a time-dependent phase transformation, the wave function evolution is shown to be governed by a spinor-component decoupled Whittaker–Hill equation. The numerical solution of these equations enables to find the quasienergy spectrum. For borophene it reveals a strong anisotropic response. By applying an extra unitary transformation, the wave functions are proven to follow an Ince equation. The evolution of the real and imaginary parts of the wave function is interpreted as the trajectory of a classical charged particle under oscillating electric and magnetic field. The topological properties of this forced quantum system are studied using this analogy. In particular, in the adiabatic driving regime, the system is described with an effective Matthieu equation while in the non-adiabatic regime the full Whittaker–Hill equation is needed. From there, it is possible to separate the dynamical and Berry phase contributions to obtain the topological phase diagram due to the driving. Therefore, a different path to perturbation theory is developed to obtain time-driven topological phases.

1. Introduction

The possibility of inducing a nontrivial topology in condensed matter systems by means of an electromagnetic drive has been the subject of many research works in recent years [1–10], some of which have focused in Dirac systems such as graphene [11–18].

More recently, two dimensional (2D) boron allotropes, also called borophenes, exhibiting Dirac cones have attracted attention due to their remarkable anisotropic properties [19–22]. In a series of previous works we studied the effects of linear [23] and elliptical [24, 25] polarized electromagnetic fields in borophene. The focus of such works was in finding the quasienergy spectrum, the associated photo currents and induced transitions, useful to design 2D electronic devices [26]. In the present work, we exploit these results and others [9, 27, 28] to study the wave function evolution and the topology induced by the interplay between an electromagnetic drive and the electrons in a Dirac system. To do so, we introduce a drive to the continuum model for a general tilted Dirac Hamiltonian. Then we use the Floquet formalism to establish the equivalence between the quantum wave function evolution and the motion of a classical charged particle in a time-dependent electromagnetic field. This is achieved through a unitary transformation that turns the

© 2022 The Author(s). Published by IOP Publishing Ltd

time-dependent Schrödinger equation into a Ince differential equation. The advantage of such formalism is that we can use previous studies of differential equations with time-dependent coefficients [29, 30]. In particular, the quantum spectrum is given by the stability charts of Mathieu's and Hill's equations and its generalizations [29]. Such equations occurs in electromagnetism, mechanics, cooling of ions, aerodynamics, marine research, biomedical engineering, celestial mechanics and general relativity [31]. Thus, the induced topological phases in the quantum problem are discussed at different regimes from the perspective of a classical orbital precession. In fact, what lays behind the analogy between quantum and classical system topology is the failure of parallel transport, which usually results in orbital precession for classical systems [32]. The archetypal example is the Focault pendulum where the phase change of its oscillating plane precession can be found as a surface integral of the Gaussian curvature of the Earth over the interior of the pendulum path [32].

In the following section we will present the model to be studied. The analogy with a classical system is presented in section 3. The topological properties are discussed in section 4, and finally, the conclusions are given.

2. Dirac materials subject to electromagnetic fields

In this section we address the model and summarize previous results concerning the Floquet theory and the quasienergy spectrum for time-driven Dirac materials [24, 33–35].

2.1. Isotropic, anisotropic and tilted Dirac materials

The most general, low-energy Dirac Hamiltonian close to one of the Dirac points, is given by [21, 23, 36, 37]

$$\hat{H} = \hbar v_t k_y \hat{\sigma}_0 + \hbar \left[v_x k_x \hat{\sigma}_x + v_y k_y \hat{\sigma}_y \right], \tag{1}$$

where k_x and k_y are the components of the two-dimensional momentum vector $\boldsymbol{k}$, $\hat{\sigma}_x$ and $\hat{\sigma}_y$ are the Pauli matrices, and $\hat{\sigma}_0$ is the 2×2 identity matrix. The Pauli matrices and $\hat{\sigma}_0$ are expressed in the sublattice basis [21]. This Hamiltonian describes, for example, $8-Pmmn$ borophene. The three velocities in the anisotropic $8-Pmmn$ borophene Dirac Hamiltonian (1) are given by $v_x = 0.86 v_F$, $v_y = 0.69 v_F$ and $v_t = 0.32 v_F$ where $v_F = 10^6\ \mathrm{m\,s^{-1}}$ [21] is the Fermi velocity. In equation (1), the last two terms give rise to the familiar form of the kinetic energy leading to the Dirac cone and the first one tilts the Dirac cone in the y direction. These two features are contained in the energy dispersion relation [24]

$$E_\eta, k = \left(\frac{v_t}{v_y} \right) \tilde{k}_y + \eta \epsilon, \tag{2}$$

where

$$\epsilon_{\boldsymbol{k}} = \sqrt{\tilde{k}_x^2 + \tilde{k}_y^2}, \tag{3}$$

and $\eta = \pm 1$ is the band index. In equation (2), we used the set of renormalized moments $\tilde{k}_x = \hbar v_x k_x$, $\tilde{k}_y = \hbar v_y k_y$. The corresponding free electron wave function is,

$$\psi_\eta(\boldsymbol{k}) = \frac{1}{\sqrt{2}} \begin{bmatrix} 1 \\ \eta \exp(i\theta_{\boldsymbol{k}}) \end{bmatrix}, \tag{4}$$

where $\theta_{\boldsymbol{k}} = \tan^{-1}(\tilde{k}_y / \tilde{k}_x)$. The case of graphene can be recovered by setting $v_t = 0$ and $v_x = v_y = v_F$ and for non-uniform strained graphene requires $v_t = 0$ and $v_x \neq v_y$.

2.2. Linearly polarized waves and Whittaker–Hill equation

Now we consider a charge carrier, described by the two-dimensional anisotropic Dirac Hamiltonian, subject to an electromagnetic wave that propagates along a direction perpendicular to the surface of the crystal. The effects of the electromagnetic field are introduced in the Dirac Hamiltonian (1) through the Peierls substitution [33, 34] $\hbar \boldsymbol{k} \to \hbar \boldsymbol{k} - e\boldsymbol{A}$ where $\boldsymbol{A} = (A_x, A_y)$ is the vector potential of the electromagnetic wave. Adopting a gauge in which $\boldsymbol{A}$ only depends on time brings a significant simplification. The Hamiltonian (1) is thus transformed into [33, 34],

$$\hat{H} = \frac{v_t}{v_y} \left(\tilde{k}_y - e v_y A_y \right) \hat{\sigma}_0 + \left(\tilde{k}_x - e v_x A_x \right) \hat{\sigma}_x + \left(\tilde{k}_y - e v_y A_y \right) \hat{\sigma}_y. \tag{5}$$

Assuming the electromagnetic wave to be linearly polarized and propagating along the z direction, the vector potential can be written as

$$\boldsymbol{A} = \frac{E_x}{\Omega}\cos(\Omega t)\hat{\boldsymbol{r}}, \tag{6}$$

where $\hat{\boldsymbol{r}} = (1,0)$ is the polarization vector, E_x is the uniform amplitude of the electric field and Ω is the angular frequency of the electromagnetic wave. It is noteworthy that the field $\boldsymbol{A}$ is not quantized and is treated classically. Thus, our results are only valid for quantum coherent field composed of a large number of photons. In the Schrödinger equation corresponding to (5),

$$i\hbar\frac{d}{dt}\boldsymbol{\Psi}(t) = \hat{H}(t)\boldsymbol{\Psi}(t), \tag{7}$$

the two dimensional spinor can be expressed as $\boldsymbol{\Psi}(t) = (\Psi_A(t), \Psi_B(t))^\top$, where A and B label the two sublattices. Formally, the solutions can be obtained from the time evolution operator $\hat{\mathcal{U}}(t)$ as,

$$\boldsymbol{\Psi}(t) = \hat{\mathcal{U}}(t)\boldsymbol{\Psi}(0). \tag{8}$$

Due to the time periodicity of the Hamiltonian $\hat{H}(t) = \hat{H}(t+T)$ where $T = 2\pi/\Omega$, solutions must comply with the Floquet theorem [33, 38] that states that the evolution operator must have the form

$$\hat{\mathcal{U}}(t) = \exp\left(-\frac{i}{\hbar}\hat{H}_e t\right)\hat{\mathcal{W}}(t), \tag{9}$$

where $\hat{\mathcal{W}}(t+T) = \hat{\mathcal{W}}(t)$ and $\hat{H}_e$ is called the effective Hamiltonian. The eigenvalues of $\hat{H}_e$ are the quasienergies of $\hat{H}(t)$,

$$\mathcal{E}_{\eta,j,m}(\boldsymbol{k}) = -\frac{\hbar\Omega}{2\pi}\arg[u_{\eta,j}(\boldsymbol{k})] + m\hbar\Omega, \tag{10}$$

where $u_{\eta,j}(\boldsymbol{k})$ are the two eigenvalues of $\hat{\mathcal{U}}(T)$, and $m = 0, \pm1, \pm2, \ldots$ and $j = 1, 2$ denote the Floquet zone and the band respectively [35].

The main challenge in deducing the wave function's explicit form resides in unraveling the coupling between the spinor components $\Psi_A(t)$ and $\Psi_B(t)$ that arise from terms proportional to $\hat{\sigma}_x$ and $\hat{\sigma}_y$ in equation (5). To uncouple the spinor components we proceed as follows. First, to transform the non-diagonal $\hat{\sigma}_x$ matrix into $\hat{\sigma}_z$, we apply a 45° rotation around the y axis of the form [35],

$$\boldsymbol{\Psi}(t) = \exp\left[-i\left(\frac{\pi}{4}\right)\hat{\sigma}_y\right]\boldsymbol{\Phi}(t). \tag{11}$$

Substituting (11) into equation (7) we obtain

$$i\frac{d}{d\phi}\boldsymbol{\Phi}(\phi) = \frac{2}{\hbar\Omega}\left[\left(\frac{v_t}{v_y}\right)\tilde{k}_y\hat{\sigma}_0 + \tilde{\Pi}_x\hat{\sigma}_z + \tilde{k}_y\hat{\sigma}_y\right]\boldsymbol{\Phi}(\phi), \tag{12}$$

where the only off-diagonal terms originate from $\hat{\sigma}_y$. In the foregoing equation, the scaled time is defined as $\phi = \Omega t/2$, the scaled momentum $\tilde{\Pi}_x = \tilde{k}_x - \zeta_x\cos(2\phi)$ and the frequency-weighted induced dipole moment is,

$$\zeta_x = \frac{ev_xE_x}{\Omega}. \tag{13}$$

The spinor components of $\boldsymbol{\Phi}(\phi) = (\Phi_+(\phi), \Phi_-(\phi))^\top$ are given by $\Phi_+(\phi) = [\Psi_A(\phi) + \Psi_B(\phi)]/\sqrt{2}$ and $\Phi_-(\phi) = [\Psi_A(\phi) - \Psi_B(\phi)]/\sqrt{2}$. Second, the term proportional to $\hat{\sigma}_0$ in equation (12) is removed by adding a time-dependent phase to the wave function

$$\boldsymbol{\Phi}(\phi) = \exp\left[-2i\left(\frac{v_t}{v_y}\right)\frac{\tilde{k}_y}{\hbar\Omega}\phi\hat{\sigma}_0\right]\boldsymbol{\chi}(\phi), \tag{14}$$

where $\boldsymbol{\chi}(\phi) = (\chi_{+1}(\phi), \chi_{-1}(\phi))^\top$. Finally, after inserting equation (14) into equation (12), differentiating both sides with respect to ϕ and using equation (12) to leave out the first order derivative, the resulting differential equation takes the form of a Whittakker–Hill equation [35, 39]

$$\boldsymbol{\chi}''(\phi) + \mathbb{F}(\phi)\boldsymbol{\chi}(\phi) = 0, \tag{15}$$

where the matrix $\mathbb{F}(\phi)$ is defined as

$$\mathbb{F}(\phi) = [a_{\boldsymbol{k}} + q_1\cos(2\phi) + q_2\cos(4\phi)]\,\hat{\sigma}_0 + iq_3\sin(2\phi)\hat{\sigma}_z. \tag{16}$$

The Whittakker–Hill equation parameters are defined as,

$$a_{\boldsymbol{k}} = \left(\frac{2\epsilon_{\boldsymbol{k}}}{\hbar\Omega}\right)^2 + 2q_0^2, \tag{17}$$

$$q_1 = -8q_0\left(\frac{\tilde{k}_x}{\hbar\Omega}\right), \tag{18}$$

$$q_2 = 2q_0^2, \tag{19}$$

$$q_3 = 4q_0, \tag{20}$$

where

$$q_0 = \frac{\zeta_x}{\hbar\Omega} = \frac{ev_xE_x}{\hbar\Omega^2}, \tag{21}$$

is the ratio between two characteristic energies of the system: the electric-field-induced dipole moment ev_x/Ω with energy ev_xE_x/Ω and the photon energy $\hbar\Omega$ [24, 40]. Thereby, $2\epsilon_{\boldsymbol{k}}/\hbar\Omega$ is the ratio of the electron kinetic energy to the photon energy, $\zeta_x/\hbar\Omega$ is the ratio of the work done on the charged carriers by the electromagnetic wave to the photon energy and $\tilde{k}_x/\hbar\Omega$ is the ratio of the x contribution of the electron kinetic energy to the photon energy.

Expressing (15) as a second order differential equation is quite advantageous for the calculations that follow. First, the evolution operator that propagates the state $\boldsymbol{\chi}(\phi)$ in time must be diagonal since $\mathbb{F}(\phi)$ is solely composed of the diagonal matrices $\hat{\sigma}_0$ and $\hat{\sigma}_z$. As a consequence of this, the scalar differential equations for the $\chi_{+1}(\phi)$ and $\chi_{-1}(\phi)$ spinor components decouple. Moreover, the differential equation for the $\chi_{-1}(\phi)$ component turns out to be the complex conjugate of the one for $\chi_{+1}(\phi)$. Both differential equations may be summarized by

$$\chi_\eta''(\phi) + [a_{\boldsymbol{k}} + q_1\cos(2\phi) + q_2\cos(4\phi) + i\eta q_3\sin(2\phi)]\,\chi_\eta(\phi) = 0, \tag{22}$$

where $\eta = \pm 1$. In principle, we can obtain the solution for $\eta = -1$ from the $\eta = +1$ solution. This is done by making the replacement $\phi \to -\phi$ in equation (22), as $\eta\sin 2\phi = \sin 2\eta\phi$. The cosines and second derivative terms are not affected by a change of sign of ϕ. Therefore, the solutions are related by,

$$\chi_{-1}(\phi) = \chi_{+1}(-\phi). \tag{23}$$

However, in general the initial conditions on the first derivative of $\chi_\eta(\phi)$ are restricted by equation (12) and thus equation (23) can only be used for $\tilde{k}_y = 0$.

We can also obtain a useful alternative expression to equation (22) by writing $\epsilon_{\boldsymbol{k}}$ in terms of the scaled moments,

$$\chi_\eta''(\phi) + 4\left[\left(\frac{\tilde{k}_x}{\hbar\Omega} - q_0\cos(2\phi)\right)^2 + \left(\frac{\tilde{k}_y}{\hbar\Omega}\right)^2 + i\eta q_0\sin(2\phi)\right]\chi_\eta(\phi) = 0. \tag{24}$$

In the previous equation, or equation (22), the spinor components are decoupled considerably simplifying the computation and the quasienergy spectrum analysis. Another gain of using this particular base is that $\chi_{+1}(\phi)$ and $\chi_{-1}(\phi)$ are the probability amplitudes of the valence and conduction bands, respectively.

In figure 1 we present the corresponding quasienergy spectrum obtained by using a very powerful numerical method developed in a previous work: the monodromy matrix method [25]. In the case of figure 1 we present the CB ($\eta = +1$) and the Floquet zone $m = 0$. This is equivalent to finding the stability regions of equation (22). Notice the two different regions in the spectrum. One is at the center where an American football ball-like shape is seen. The other, in the outer regions of the spectrum, exhibits concentric circles. As we will discuss, the nature of such regions can be identified by looking at the different behaviors in equation (22) depending on its coefficient values. However, it is useful to consider first how these coefficients are related with the physics of the system. For example, in $a_{\boldsymbol{k}}$ appears the ratio between twice the energy of

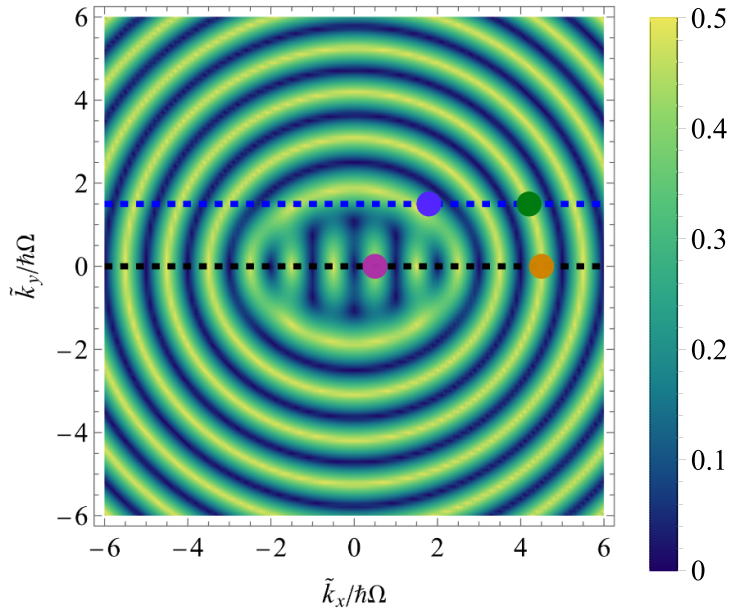

Figure 1. Density plot of quasienergy spectrum $\mathcal{E}_{\eta,j,m}/(\hbar\Omega) - v_i\tilde{k}_y/(v_y\hbar\Omega)$ for $\eta = +1$ and $m = 0$ as a function of $\tilde{k}_x/\hbar\Omega$ and $\tilde{k}_y/\hbar\Omega$. The amplitude and frequency of the electromagnetic wave are $E_x = 4.5\ \mathrm{V\,m^{-1}}$ and $\Omega = 50 \times 10^9$ Hz. The horizontal dashed black and blue lines correspond to fixed values $\tilde{k}_y/\hbar\Omega = 0$ and $\tilde{k}_y/\hbar\Omega = 1.5$, respectively. The dots are the states that were chosen to produce the trajectories in figures 2 and 3.

the electrons ($2\epsilon_{\boldsymbol{k}}$) and the energy of a photon ($\hbar\Omega$). If for a given $\boldsymbol{k}$ we consider the difference in energy between the valence and conduction band, it turns out to be precisely $2\epsilon_{\boldsymbol{k}}$. Moreover, we can consider that for such $\boldsymbol{k}$ the system behaves as a driven two-level system, akin to the Rabi problem. Therefore, transitions between states will not be produced whenever the field is such that $2\epsilon_{\boldsymbol{k}}/\hbar\Omega > 1$. But if transitions are observed, the system is considered as non-adiabatic [41]. By looking at equation (3) we can relate the non-adiabatic condition with a region of $\tilde{\boldsymbol{k}}$ around the origin. A second condition for having adiabaticity is that E_x must be small in order to have a perturbation. As E_x only enters in q_0 and by taking into account all these previous considerations, the condition that defines the crossover between the adiabatic and non-adiabatic regimes is given by,

$$\epsilon_{\boldsymbol{k}} \approx \zeta_x = \hbar\Omega q_0. \tag{25}$$

It turns out that this condition coincides with the, numerically found, ball limit seen in figure 1. Therefore, we conclude that outside the ball the system can be considered in a weak interaction regime where the quasienergy spectrum is almost similar to the non-perturbed energy dispersion as expected .

It is worthwhile to observe that for Dirac systems there is no gap, and thus this is the only way to give a meaning to a topological phase as in the presence of an external field there is always a small region near the Dirac point where these transitions are observed. This is testified by the fact that the optical absorption of graphene is flat with respect to the field frequency. Usually, this condition is ignored and an arbitrary trajectory in $\boldsymbol{k}$-space is used to find the Chern number without any further reflection about the limits of its use.

Let us then consider three different regimes: the adiabatic ($ev_xE_x/\hbar\Omega^2 < 1$), the non-adiabatic ($ev_xE_x/\hbar\Omega^2 > 1$) and the transitional ($ev_xE_x/\hbar\Omega^2 \approx 1$) regimes. In figures 2(b), (e), and 3(b), we present the evolution of the real and imaginary parts of the first spinor component $\chi_{+1}(\phi)$ for states chosen at different points of the Borophene's quasienergy spectrum. These states, indicated with dots in figure 1, correspond to the four most representative cases listed below:

(a) Adiabatic regime with $\tilde{k}_y \neq 0$ (green dot),
(b) Non-adiabatic regime with $\tilde{k}_y = 0$ (purple dot),
(c) Non-adiabatic regime with $\tilde{k}_y \neq 0$ (blue dot),
(d) Transitional regime with $\tilde{k}_y = 0$ (orange dot).

The trajectories seen in figures 2(b) and (e), 3(b) and (e) were obtained from a numerical simulation made by solving equation (22). As the initial state, we chose a band eigenstate of the time-independent

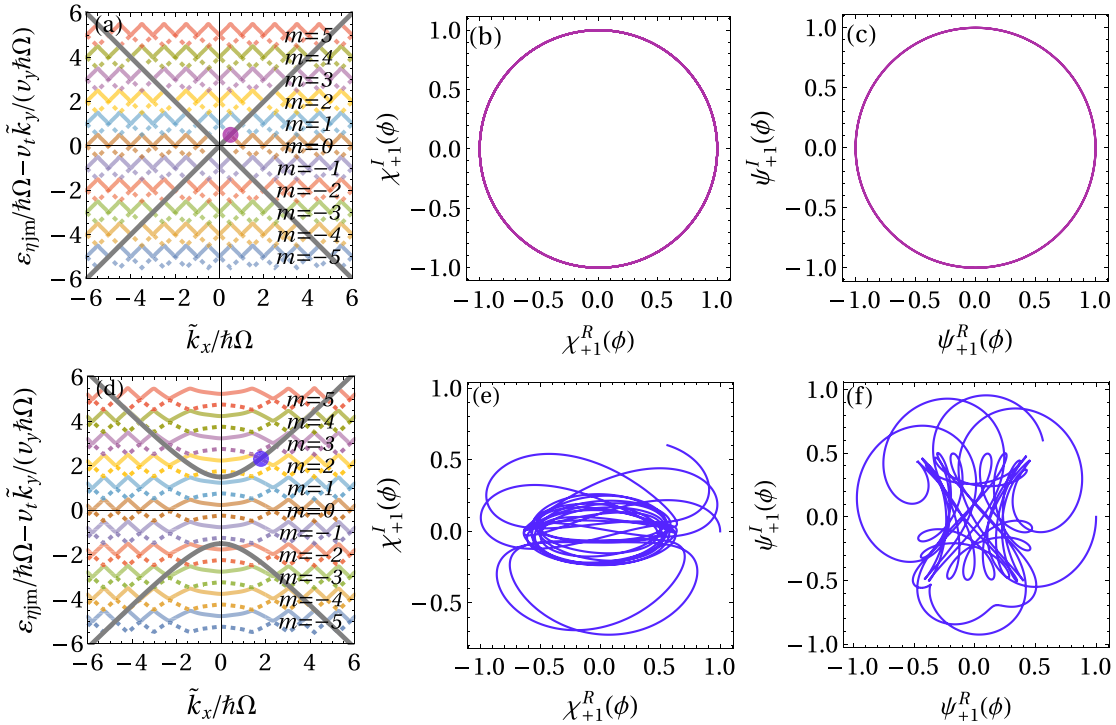

Figure 2. Quasienergy spectrum $\mathcal{E}_{\eta,j,m}/(\hbar\Omega) - v_t\tilde{k}_y/(v_y\hbar\Omega)$ and the Floquet quantum wave real and imaginary part for the Wittaker–Hill and Ince equations. In panels (a) and (d), we show the quasienergy spectra as a function of the momentum $\tilde{k}_x/\hbar\Omega$ using the fixed values $\tilde{k}_y/\hbar\Omega = 0$ and $\tilde{k}_y/\hbar\Omega = 1.5$ for $j = 1, 2$ and $m = 0, \pm1, \ldots, \pm5$ (Floquet zones), respectively. In these panels, the purple dot correspond to the state where $(\tilde{k}_x/\hbar\Omega,\ \mathcal{E}_{\eta,j,m}/(\hbar\Omega) - v_t\tilde{k}_y/(v_y\hbar\Omega)) = (0.50, 0.50)$ and the corresponding blue dot is the state $(\tilde{k}_x/\hbar\Omega,\ \mathcal{E}_{\eta,j,m}/(\hbar\Omega) - v_t\tilde{k}_y/(v_y\hbar\Omega)) = (1.79, 2.31)$. The solid gray lines correspond to the dispersion relation given by equation (3) for fixed $\tilde{k}_y/\hbar\Omega$ values mentioned above. In panels (b) and (c), we show the trajectories for the Whittaker–Hill and Ince equations for $\eta = +1$ and $(\tilde{k}_x/\hbar\Omega,\ \mathcal{E}_{\eta,j,m}/(\hbar\Omega) - v_t\tilde{k}_y/(v_y\hbar\Omega)) = (0.5, 0.50)$, respectively. The panels (e) and (f) are the corresponding trajectories for $\eta = +1$ and $(\tilde{k}_x/\hbar\Omega,\ \mathcal{E}_{\eta,j,m}/(\hbar\Omega) - v_t\tilde{k}_y/(v_y\hbar\Omega)) = (1.79, 2.31)$. In all these panels the value of amplitude and frequency of the electromagnetic wave are $E_x = 4.85\ \mathrm{V\,m^{-1}}$ and $\Omega = 50 \times 10^9$ Hz, corresponding to $q_0 = 2.35$. Observe how trajectories with $\tilde{k}_y/\hbar\Omega = 0$ describe circles in agreement with equation (26).

problem. Since (22) is a second order differential equation, it requires an additional initial condition that comes from the first derivative of the wave function in equation (12). In figures 2(a) and (d), 3(a) and (d) we indicate the chosen states in several quasi spectrum cross sections. The Floquet zone replicas are also tagged. We have confirmed that these solutions for the wave functions as well as the quasienergy spectrum are consistent with the ones obtained via the time-independent effective Hamiltonian ensued by the monodromy matrix [25]. In [42], the weak-field and high-frequency regime was studied for graphene. We have verified that numerically, our obtained solutions are equal to those of [42]. For the particular case $\tilde{k}_y = 0$ ($k_y = 0$), the analytical solution given in [42] is identical to our equations (26) and (27).

From figures 2(b) and (e), 3(b) and (e), we observe that as the wave functions evolve their real and imaginary parts may either move along complex paths or even describe simple circular trajectories. In particular, in figures 2(b) and 3(b), the real and imaginary parts of the wave function describe circular paths. This can be understood from equation (24), or more directly from equation (12), as in this case $\tilde{k}_y = 0$ the spinor components are decoupled right from the beginning and there is no need to go into the second derivative calculation. Thus, $\boldsymbol{\chi}(\phi) = (\chi_{+1}(\phi), \chi_{-1}(\phi))$ and the solution is,

$$\chi_\eta(\phi) = \chi_\eta(0)\exp\left[2i\eta\int_0^\phi\left(q_0\cos(2\phi') - \frac{\tilde{k}_x}{\hbar\Omega}\right)d\phi'\right], \tag{26}$$

or using that in this case $\epsilon_{\boldsymbol{k}} = \tilde{k}_x$ and $\phi = \Omega t/2$, we obtain that,

$$\chi_\eta(t) = \chi_\eta(0)\exp\left[i\eta\left(q_0\sin(\Omega t) - \frac{\epsilon_{\boldsymbol{k}}t}{\hbar}\right)\right]. \tag{27}$$

The real and imaginary parts of this solution describe the circular paths shown in figures 2(b) and 3(b). What is remarkable here is that equation (27) holds in the non-adiabatic, the adiabatic and the transitional

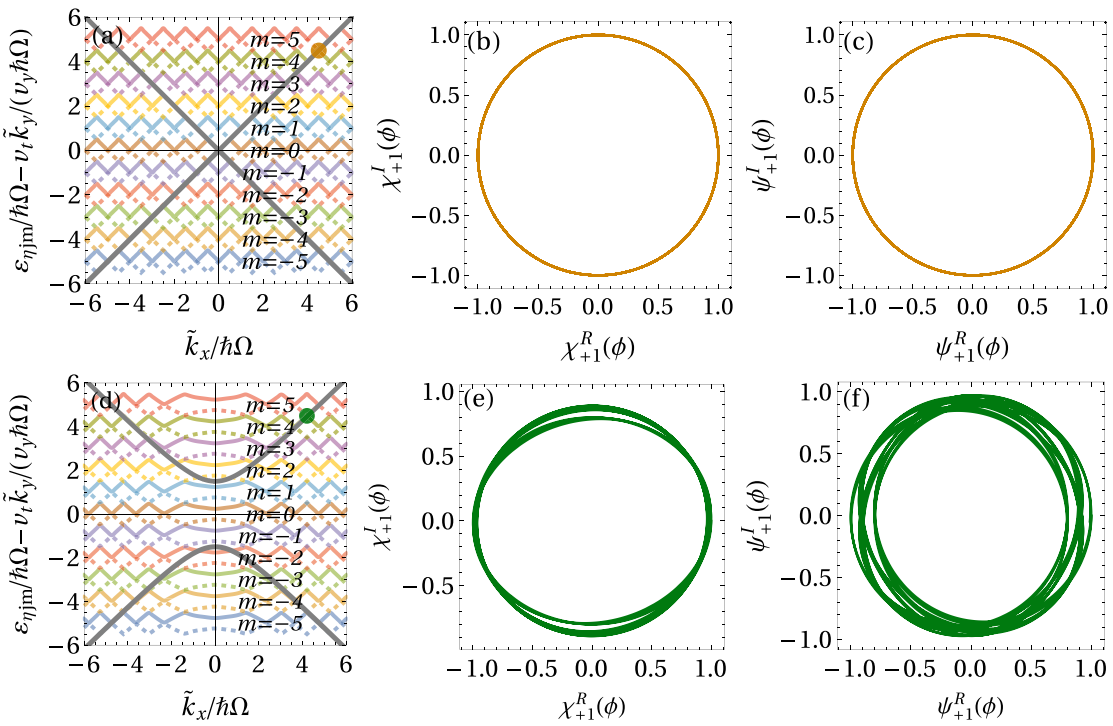

Figure 3. Quasienergy spectrum $\mathcal{E}_{\eta,j,m}/(\hbar\Omega) - v_t\tilde{k}_y/(v_y\hbar\Omega)$ and the Floquet quantum wave real and imaginary part for the Wittaker–Hill and Ince equations. In panels (a) and (d), we show the quasienergy spectra as a function of the momentum $\tilde{k}_x/\hbar\Omega$ using the fixed values $\tilde{k}_y/\hbar\Omega = 0$ and $\tilde{k}_y/\hbar\Omega = 1.5$ for $j = 1, 2$ and $m = 0, \pm1, \ldots, \pm5$ (Floquet zones), respectively. In these panels, the orange dot correspond to the state where $(\tilde{k}_x/\hbar\Omega,\ \mathcal{E}_{\eta,j,m}/(\hbar\Omega) - v_t\tilde{k}_y/(v_y\hbar\Omega)) = (4.5, 4.5)$ and the corresponding green dot is the state $(\tilde{k}_x/\hbar\Omega,\ \mathcal{E}_{\eta,j,m}/(\hbar\Omega) - v_t\tilde{k}_y/(v_y\hbar\Omega)) = (4.2, 4.49)$. The solid gray lines corresponds to the dispersion relation given by equation (3) for fixed $\tilde{k}_y/\hbar\Omega$ values mentioned above. In panels (b) and (c), we show the trajectories for the Whittaker–Hill and Ince equations for $\eta = +1$ and $(\tilde{k}_x/\hbar\Omega,\ \mathcal{E}_{\eta,j,m}/(\hbar\Omega) - v_t\tilde{k}_y/(v_y\hbar\Omega)) = (4.5, 4.5)$, respectively. The panels (e) and (f) are the corresponding trajectories for $\eta = +1$ and $(\tilde{k}_x/\hbar\Omega,\ \mathcal{E}_{\eta,j,m}/(\hbar\Omega) - v_t\tilde{k}_y/(v_y\hbar\Omega)) = (4.2, 4.49)$. In all these panels the value of amplitude and frequency of the electromagnetic wave are $E_x = 4.85\ \mathrm{V\,m^{-1}}$ and $\Omega = 50 \times 10^9$ Hz, corresponding to $q_0 = 2.35$. Observe how trajectories with $\tilde{k}_y/\hbar\Omega = 0$ describe circles in agreement with equation (26).

regime, i.e. it covers items (b) and (d) of the list of most representative cases. As we will see in the following section, this allows to characterize the Berry phase in a simple way.

Now let us return to the case where in equation (18) $\tilde{k}_x \neq 0$ and $\tilde{k}_y \neq 0$ but $q_1 \gg q_0^2$. Under these conditions the solution of equation (18) requires setting $\tilde{k}_x \gg q_0\hbar\Omega$ from where $\epsilon_{\boldsymbol{k}} \gg \hbar\Omega q_0$. According to equation (25) such a case corresponds to states well inside the adiabatic regime. Using equation (19) we neglect q_2 and equation (24) takes the form

$$\chi_\eta''(\phi) + [a_{\boldsymbol{k}} + q_1\cos(2\phi) + i\eta q_3\sin(2\phi)]\,\chi_\eta(\phi) = 0. \tag{28}$$

This is a generalized Matthieu equation [29], but if we further assume that $\tilde{k}_x \gg \hbar\Omega/2$ and therefore photons are far from inducing transitions, then equation (22) transforms into a simple Matthieu equation as $q_1 \gg q_0$ giving

$$\chi_\eta''(\phi) + [a_{\boldsymbol{k}} + q_1\cos(2\phi)]\,\chi_\eta(\phi) = 0. \tag{29}$$

This very well known equation describes a pendulum with time-driven variable length, or alternatively, an harmonic oscillator with natural frequency $\sqrt{a_{\boldsymbol{k}}}$ with a periodically perturbed time-dependent spring constant variation $-q_1\cos(2\phi)$. The physical relevant solutions are given by a stability chart in the $a_{\boldsymbol{k}}$ and q_1 parameter space, divided in forbidden and allowed regions [29]. Resonances appear around $\sqrt{a_{\boldsymbol{k}}} = n$ with n integer. In this quantum context, the forbidden regions correspond to the spectral gaps as they represent non-physical runaway solutions. Each resonance defines the limit of the Floquet zone. Including the initial conditions, the solutions are given by,

$$\chi_-(\phi) = \frac{\mathcal{C}\left(a_{\boldsymbol{k}}, -\frac{q_1}{2}, \phi\right)}{\mathcal{C}\left(a_{\boldsymbol{k}}, -\frac{q_1}{2}, 0\right)} - \frac{2i\left(\tilde{k}_x - \hbar\Omega q_0\right)\mathcal{S}\left(a_{\boldsymbol{k}}, -\frac{q_1}{2}, \phi\right)}{\hbar\Omega\mathcal{S}'\left(a_{\boldsymbol{k}}, -\frac{q_1}{2}, 0\right)}, \tag{30}$$

$$\chi_+(\phi) = \frac{2\tilde{k}_y \mathcal{S}\left(a_{\boldsymbol{k}}, -\frac{q_1}{2}, \phi\right)}{\hbar\Omega \mathcal{S}'\left(a_{\boldsymbol{k}}, -\frac{q_1}{2}, 0\right)}, \tag{31}$$

where $\mathcal{C}(a_{\boldsymbol{k}}, -q_1/2, \phi)$ and $\mathcal{S}(a_{\boldsymbol{k}}, -q_1/2, \phi)$ are the Mathieu cosine and sine functions, respectively. The first derivatives of the Mathieu functions are $\mathcal{C}'(a_{\boldsymbol{k}}, -q_1/2, \phi) = (d/d\phi)\mathcal{C}(a_{\boldsymbol{k}}, -q_1/2, \phi)$ and $\mathcal{S}'(a_{\boldsymbol{k}}, -q_1/2, \phi) = (d/d\phi)\mathcal{S}(a_{\boldsymbol{k}}, -q_1/2, \phi)$. Aside from the initial conditions ensued by equation (12), in the previous equations we have also assumed that $\chi_{+1}(0) = 0$ and $\chi_{-1}(0) = 1$ which means that initially the electron is in the valence band. The quasienergies are obtained by using the Fourier expansion of such functions. This is a very interesting result as in the adiabatic regime we have both the oscillator's fundamental frequency and the oscillating drive's frequency. Such two frequencies are reflected in the orbital precession seen in figures 3(e) and (f). As we will discuss, our results must be akin to those of Thouless concerning adiabatic phases and thus Berry topology. However, here we arrived to such result not by perturbation theory but from a non-perturbative approach. Moreover, our generalized Whittaker–Hill equation (22) allows to find extra contributions and explore non-adiabatic regimes.

Also, the previous analysis of particular cases opens the question whether for $q_3 \neq 0$ we can develop a suitable classical analogy to the quantum equations. This is the subject of the following section.

3. Ince equation: quantum wave functions as classical trajectories under electromagnetic fields

The previous section showed how a quantum wave function evolution of a time-driven system can be described in some particular cases by a simple classical problem. In this section we show how to fully extend the analogy to a classical system. In particular, we study the trajectories that arise when the Whittaker–Hill equation (15) is transformed into the Ince equation. Consider the following unitary transformation

$$\chi_\eta(\phi) = \exp\left[i\eta q_0 \sin(2\phi)\right]\psi_\eta(\phi), \tag{32}$$

Substituting this last expression into equation (15), turns the Wittaker–Hill equation into a Ince equation for $\psi_\eta(\phi)$, i.e.

$$\psi_\eta''(\phi) + if_\eta(\phi)\psi_\eta'(\phi) + g(\phi)\psi_\eta(\phi) = 0, \tag{33}$$

where

$$f_\eta(\phi) = \eta|q_3|\cos(2\phi), \tag{34}$$

$$g(\phi) = \left(\frac{2\epsilon_{\boldsymbol{k}}}{\hbar\Omega}\right)^2 + q_1\cos(2\phi). \tag{35}$$

There are two advantages of the transformation given by equation (32). One is evident by comparing with equation (26), as it separates the contribution that comes from $\tilde{k}_x$ whenever $\tilde{k}_y = 0$. But what is more important here is the possibility of finding a suitable classical analogy. Although this can be done in the Whitaker–Hill equation, the resulting fields are far from simple known physical cases. The solution of the Ince differential equation can be decomposed into its real part and its imaginary part, that is, $\psi_\eta(\phi) = \psi_\eta^R(\phi) + i\psi_\eta^I(\phi)$, and we find the following set of coupled differential equations

$$\frac{d^2}{d\phi^2}\psi_\eta^R(\phi) - f_\eta(\phi)\frac{d}{d\phi}\psi_\eta^I(\phi) + g(\phi)\psi_\eta^R(\phi) = 0, \tag{36}$$

$$\frac{d^2}{d\phi^2}\psi_\eta^I(\phi) + f_\eta(\phi)\frac{d}{d\phi}\psi_\eta^R(\phi) + g(\phi)\psi_\eta^I(\phi) = 0. \tag{37}$$

Let us now explore the classical analogy. We propose the following replacement $\psi_\eta^R(\phi) \to X(\phi)$, $\psi_\eta^I(\phi) \to Y(\phi)$. Notice that to keep the derivation simple, we drop η and then quote the result for $\eta = -1$ at the end of the calculation. The resulting Ince equations are written as,

$$\frac{d^2X(\phi)}{d\phi^2} - f_\eta(\phi)\frac{d}{d\phi}Y(\phi) + g(\phi)X(\phi) = 0, \tag{38}$$

$$\frac{d^2Y(\phi)}{d\phi^2} + f_\eta(\phi)\frac{d}{d\phi}X(\phi) + g(\phi)Y(\phi) = 0. \tag{39}$$

Consider the problem of classical particle with mass m and charge Q moving in a plane under an electromagnetic field given by a radial time dependent electric field,

$$\mathbf{E}(\mathbf{t}) = -\frac{g(t)}{Q}\mathbf{r}, \tag{40}$$

with $\mathbf{r} = (X, Y, 0)$ the position vector and a perpendicular time dependent magnetic field,

$$\mathbf{B}(\mathbf{t}) = \frac{f(t)}{Q}\hat{\mathbf{k}}, \tag{41}$$

with $\hat{\mathbf{k}} = (0, 0, 1)$. The classical particle equation of motion is,

$$m\frac{d^2\boldsymbol{r}}{dt^2} = Q\boldsymbol{E}(t) + Q\boldsymbol{v} \times \boldsymbol{B}(t), \tag{42}$$

with $\boldsymbol{v} = d\boldsymbol{r}/dt$. The equation for the other valley is obtained by reversing the direction of the magnetic field in the $-\hat{\mathbf{k}}$ direction.

Comparing the set of differential equations (38) and (39) arising from Ince equation with the equation (42) of a charged particle motion problem we see that they are similar. The classical problem of the charged particle in presence of a time-dependent electromagnetic fields with axial symmetry was studied long time ago by using the Lewis–Riesenfeld invariant theory [43, 44]. The Lorentz force equation (42) does not have the exactly same time-dependent axial symmetry as those in such classical works, therefore we can not compare both cases directly. However, we can visualize the phase of the wave function and ask what is the relationship between such trajectories and the topological properties of the wave function phases. This is the subject of the following section.

4. Topological phases of Dirac systems under linearly polarized light

As is well known, the initial spark in the study of topological phases was the discovery by Berry [45] that a quantum system subjected to an adiabatic change in its parameters gets a geometrical phase γ_B in the wave function evolution, known as the Berry phase [46, 47]. This phase, which due to the Floquet theorem must be $\gamma_B = 2\pi n$ with n an integer when a closed path is made with the parameters (where the case $n = 0$ is considered as topologically trivial), adds to the dynamical phase determined by the instantaneous eigenvalues $\bar{\epsilon}_{\boldsymbol{k}}(\boldsymbol{A}(t))$ of the Hamiltonian, i.e. the total wave-function is,

$$\psi_{\boldsymbol{k}}(t) = \exp\left[i\gamma_B(t)\right]\exp\left[-\frac{i}{\hbar}\int_0^t \bar{\epsilon}_{\boldsymbol{k}}(t')dt'\right]|\boldsymbol{k}(\boldsymbol{A}(t))\rangle, \tag{43}$$

where $|\boldsymbol{k}(\boldsymbol{A}(t))\rangle$ is an instantaneous eigenvector which satisfies,

$$\hat{H}(t)|\boldsymbol{k}(t)\rangle = \bar{\epsilon}_{\boldsymbol{k}}(\boldsymbol{A}(t))|\boldsymbol{k}(\boldsymbol{A}(t))\rangle, \tag{44}$$

and $\gamma_B(t)$ is the geometrical phase at time t such that,

$$\gamma_B = \gamma_B(T) - \gamma_B(0). \tag{45}$$

The argument $\boldsymbol{A}(t)$ appears here to highlight the parameter that performs the external driving. Therefore, the total phase obtained by the wavefunction after a one-cycle drive is,

$$\gamma_{\boldsymbol{k}}(T) = \gamma_B + \gamma_D(T), \tag{46}$$

where we defined the dynamical phase as,

$$\gamma_D(t) = \int_0^t \bar{\epsilon}_{\boldsymbol{k}}(t')dt'. \tag{47}$$

In our system,

$$\bar{\epsilon}_{\boldsymbol{k}}(\phi) = \pm\sqrt{\left(\frac{\tilde{k}_x}{\hbar\Omega} - q_0\cos(2\phi)\right)^2 + \left(\frac{\tilde{k}_y}{\hbar\Omega}\right)^2}. \tag{48}$$

As equation (24) allows to find the total wave function and $\gamma_D(t)$ is easy to find, it is clear that in principle we can recover the Berry phase from $\gamma_B = \gamma_{\boldsymbol{k}}(T) - \gamma_D(T)$. Although such definition works for adiabatic and non-adiabatic cases, in the non-adiabatic case the phase is not necessarily geometric. However, in the adiabatic regime $\gamma_B(t)$ coincides with the usual definition of Berry phase.

Consider as an example the case $\tilde{k}_y = 0$. The analytical solution equation (26) can be written as,

$$\chi_{\pm 1}(t) = \chi_{\pm 1}(0) \exp\left[-\frac{i}{\hbar}\int_0^t \bar{\epsilon}_{\boldsymbol{k}}(t')dt'\right]. \tag{49}$$

By comparing with equation (43), we conclude that $\gamma_B = 0$ implying that in the line $\tilde{k}_y = 0$ the system is topologically trivial. This explains why in a previous work, it was found numerically that states at such line do not have transitions to other states, even at very high fields [25]. Mathematically, such a result follows from a special condition that the instantaneous eigenvalues satisfy for $\tilde{k}_y = 0$,

$$\frac{d\bar{\epsilon}_{\boldsymbol{k}}(\phi)}{d\phi} = 2q_0 \sin 2\phi, \tag{50}$$

and from where the Whittaker–Hill equation is,

$$\chi_\eta''(\phi) + \left[4\bar{\epsilon}_{\boldsymbol{k}}^2(\phi) - i2\eta\frac{d\bar{\epsilon}_{\boldsymbol{k}}(\phi)}{d\phi}\right]\chi_\eta(\phi) = 0. \tag{51}$$

Meanwhile, from equation (43) it is clear that the classical trajectories are circular in the Whittaker–Hill and Ince pictures, as in this case the resulting equations are similar. Therefore, topologically trivial phases are given by circular trajectories. Intuitively, such result is to be expected as for trivial topological phases there is not a sort of 'phase leaking' to higher energy states. Physically, as linear polarized light is made from a superposition of the same amount of left and right photon polarization, due to momentum conservation, transitions are forbidden if the electron does not have momentum in a perpendicular direction to $\boldsymbol{A}(\boldsymbol{r})$.

Now consider the adiabatic regime for $\tilde{k}_y \neq 0$. Such conditions corresponds to item (a) of the list of most representative cases and to the green dot in the quasi-energy spectrum of figure 1. In this limit, the solution is determined by the pure Mathieu equation (29) and the initial conditions. Following Thouless [41], we consider that at $\phi = 0$ ($t = 0$) the system is in a pure valence band state of the stationary problem. According to equation (30), this is translated into $\chi_{+1}(0) = 0$ and $\chi_{-1}(0) = 1$. Notice here that due to the properties of the Mathieu sine function, $\mathcal{S}'(a_{\boldsymbol{k}}, -q_1/2, 0) \neq 0$ and thus the denominator of $\chi_{+1}(\phi) = 0$ is well defined. For $\tilde{k}_y \neq 0$ we see from equation (30) that $\chi_{+1}(\phi)$ can be different from zero as time evolves. As a consequence, for $\tilde{k}_y \neq 0$ there will be a small projection onto the conduction band. This is the hallmark of a topological phase. To understand this, here we quote the result by Thouless applied to a time-driven two level system [41]. In the absence of a field, the ground state has an energy ε_0 and a high energy state an energy ε_1. If the system is at the ground state for $t = 0$, in the adiabatic regime the time evolution of the wave function is [41],

$$|\psi(t)\rangle \approx e^{-\frac{i}{\hbar}\int_0^t \epsilon_1(t')dt'}\left(|\psi_0(t)\rangle + |\psi_1(t)\rangle\frac{i\hbar\langle\psi_2(t)|\dot{\psi}_1(t)\rangle}{\epsilon_1(t) - \epsilon_0(t)}\right) \tag{52}$$

where $\psi_0(t)$ and $\psi_1(t)$ are the instantaneous states of the time dependent two-level Hamiltonian, each with instantaneous energies $\epsilon_0(t)$ and $\epsilon_1(t)$ respectively. The second term of equation (52) is the projection into the high-energy state and gives the extra geometrical phase [41]. This solution is meant to be compared with equation (30), showing that the second term is a projection of the time evolution into the high-energy state. Notice that the Mathieu functions $\mathcal{C}\left(a_{\boldsymbol{k}}, -\frac{q_1}{2}, \phi\right)$ and $\mathcal{S}\left(a_{\boldsymbol{k}}, -\frac{q_1}{2}, \phi\right)$ already contain in their definition the integral in time of the quasi-energy, as they have the general form $e^{i\mu(a_k, -q_1/2, \phi)}F(a_k, -q_1/2, \phi)$, where $F(a_k, -q_1/2, \phi)$ is a polynomial and $\mu(a_k, -q_1/2, \phi)$ is the Floquet exponent [35, 48]. The small projection of the solution into the high energy state can be seen in figures 3(e) and (f) as an orbital precession due to the two frequencies involved. Thus, the topology is reflected in an orbital precession of the phase, in agreement with the general expected result for classical systems [32].

Moreover, to further understand how equation (30) is related with the topology, we remark that such equation is consistent for $\tilde{k}_y = 0$, as for this case $\chi_{+1}(\phi) = 0$ at all times and thus the system has no projection in the conduction band resulting in a trivial topology. As there is no projection into the upper state, the phase describes circular trajectories.

Finally, for the non-adiabatic $\tilde{k}_y \neq 0$ case (blue dot state), the classical trajectories are far from circles as the conduction band component is not small and in fact transitions are induced. Moreover, the full Whittaker–Hill equation is needed as in this case the term q_2, which corresponds to a doubling of the drive

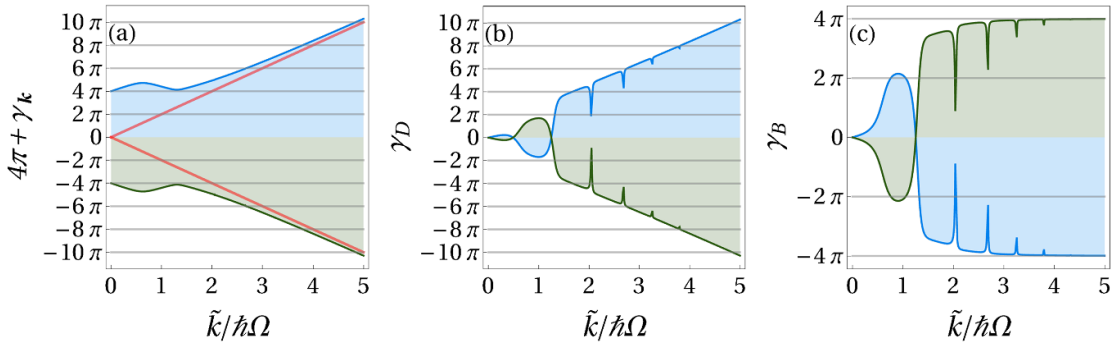

Figure 4. Numerically obtained $\Psi_k(t)$ phases for $\tilde{\boldsymbol{k}}_y \neq 0$: (a) quasienergy, (b) dynamical phase and (c) Berry phase as functions of the momentum $\tilde{k} = \sqrt{\tilde{k}_x^2 + \tilde{k}_y^2}$ where $\tilde{k}_x = \tilde{k}\cos(\pi/4)$ and $\tilde{k}_y = \tilde{k}\sin(\pi/4)$. The intensity of the electric field is $E_x = 4.5\ \mathrm{V\,m^{-1}}$ and $\Omega = 5 \times 10^9$ Hz. The solid blue and green lines correspond to the positive and negative eigenvalues, respectively. The solid red lines in panel (a) indicate the free electron eigen energies. For $\tilde{k} > ev_x E_x/\hbar\Omega^2$, corresponding to states outside the ball, the Berry phase saturates into a non-trivial phase which corresponds to the result obtained in the adiabatic case. However, inside the non-adiabatic region, many new different field-induced phases are seen.

frequency, will dominate. Not surprisingly, the same equation appears in the calculation of celestial bodies orbital precession [31].

So far we have calculated the Berry phase for regimes that allow an analytical solution: mainly $\tilde{k}_y = 0$, the adiabatic approximation and $q_1 \gg q_0^2$. Obtaining the Berry phase in the general case requires further analysis. The main difficulty that arises for the most general Hamiltonian is the non-adiabaticity of the electric field near the Dirac point. Fortunately the adiabatic restriction was first removed by Aharonov and Anadan in their pioneering work [49] and then new ways of working out non-adiabatic Berry phases were developed by Page [50] and later on by Moore [51, 52]. Even though we have performed the calculation of the non-adiabatic Berry phases using the approaches by Moore and Page obtaining identical results, here we only present the one corresponding to [50] because it is not restricted to Floquet states. According to this standpoint, the non-adiabatic Berry and dynamical phases can be computed through

$$\gamma_B(T) = \frac{i}{2}\oint_C \frac{w^* dw - w dw^*}{1+|w|^2}, \tag{53}$$

$$\gamma_D(T) = -\int_0^T \boldsymbol{\Psi}^\dagger(t)\hat{H}(t)\boldsymbol{\Psi}(t)dt, \tag{54}$$

where $w = \Psi_B(t)/\Psi_A(t)$ and C is the closed contour of w and w^* described through one period T of time evolution. The wave function components $\Psi_A(t)$ and $\Psi_B(t)$ where worked back from the solution of the Ince equation through the transformations (11) and (14). Figure 4 shows the quasienergy phase $\gamma_{\boldsymbol{k}}(T)$ (a), the dynamical phase $\gamma_D(T)$ (b) and the non-adiabatic Berry phase $\gamma_B(T)$ (c) as a functions of the momentum $\tilde{k}/\hbar\Omega$ along a line at 45° with respect to the $\tilde{k}_x$ axis. The straight (red) lines in figure 4(a) correspond to the free electron energy spectrum. The positive (negative) quasienergie phases were shifted to higher (lower) Floquet zones in order to demonstrate that far from the Dirac point the free electron energy spectrum is recovered. The dynamical (figure 4(b)) and Berry (figure 4(c)) phases where shifted accordingly. In this way, these figures one can readily verify equation (46) by adding an extra phase of 4π to the quasienergy $\gamma_{\boldsymbol{k}}(T)$. We must first note that the limiting cases of the Berry phase where $\tilde{k}_y = 0$, $\tilde{k}$ and $\tilde{k} \gg ev_x E_x/\Omega$ coincide with the above obtained analytical results. The truly interesting Berry phases arise in the non-adiabatic region $0 < \tilde{k} < ev_x E_x/\Omega$ where γ_B smoothly varies between 0 and $\pm 4\pi$.

The question of why $\gamma_B \neq \pi$ remains to be answered. Though a more thorough analysis is needed in order to fully answer this question we can venture two possible scenarios that lead to more complicated Berry phases. First, in the vicinity of the Dirac point the wave function is heavily distorted as figure 1 suggests. Additionally, in this region the adiabatic condition does not hold. Therefore we cannot expect the Berry phase to be equal to π. Moreover, one could argue that far from the Dirac point where the adiabatic condition holds we should recover $\gamma_B = \pi$. However, since close to the Dirac point the wave function is strongly modified by the oscillating electric field, we can expect that the phase singularity that yields $\gamma_B = \pi$ is either lifted or canceled by the appearance of new ones. In the second scenario, the integration path of the Berry phase could even avoid the Dirac point. For non-adiabatic time-dependent fields the path followed by the wave function is determined by the dynamics of the system as equation (53) states. Even though under

these conditions the Berry phase is still geometrical in nature, it is difficult to tell which path is taken by the wave function components during the evolution of the system. Therefore, a deeper analysis of the Berry phase should include the determination of the shapes of the paths followed by the wave function in k-space as well as the alterations of the features of the phase singularities, if any, of the modified wave function close to the Dirac point.

5. Conclusions

The time evolution of an electron in a 2D Dirac material driven by linear polarized electromagnetic fields was found using Floquet theory. In particular, the bispinor wave function time evolution was reduced to an ordinary Whittaker–Hill differential equation by using several transformations. The resulting trajectories for the phases were obtained numerically and in some cases, it was possible to compare with the analytical results.

Then we described the phase of the electron wave function as a classical charged particles in a time-driven electromagnetic field. This is particularly clear if a transformation is made into the Ince equation. Circular trajectories were thus identified as trivial topological phases. This occurs when the electron momentum is aligned with the photon momentum and transitions are forbidden. When this is not the case, non-trivial topological phases were identified as trajectories with orbital precession. They are described by a Mathieu equation and the precession is due to a phase leaking into the conduction band states. In the non-adiabatic regime, the trajectories are complicated except for the case in which electrons and photons have parallel momentum. Such result is due to the role played by a frequency component that doubles the original driving frequency. Finally, the Berry phase was obtained from the dynamical evolution of the system.

Data availability statement

All data that support the findings of this study are included within the article (and any supplementary files).

Acknowledgments

This work was supported by DCB UAM-A Grant Numbers 22322014, and UNAM DGAPA PAPIIT IN102620, and CONACyT Project 1564464. S A H acknowledges financial support from CONACyT. J C S S and V G I S acknowledge the total support from Estancias Posdoctorales por México 2021 CONACYT.

ORCID iDs

V G Ibarra-Sierra https://orcid.org/0000-0003-2416-3261
J C Sandoval-Santana https://orcid.org/0000-0002-1166-4529
A Kunold https://orcid.org/0000-0003-1545-8017
Saúl A Herrera https://orcid.org/0000-0001-7404-9630
Gerardo G Naumis https://orcid.org/0000-0002-1338-1522

References

[1] Bao C, Tang P, Sun D and Zhou S 2021 Light-induced emergent phenomena in 2D materials and topological materials *Nat. Rev. Phys.* **4** 33–48
[2] Lindner N H, Refael G and Galitski V 2011 Floquet topological insulator in semiconductor quantum wells *Nat. Phys.* **7** 490–5
[3] Rudner M S and Lindner N H 2020 Band structure engineering and non-equilibrium dynamics in Floquet topological insulators *Nat. Rev. Phys.* **2** 229–44
[4] Seetharam K I, Bardyn C-E, Lindner N H, Rudner M S and Refael G 2015 Controlled population of Floquet–Bloch states via coupling to Bose and Fermi baths *Phys. Rev.* X **5** 041050
[5] Gómez-León A and Platero G 2013 Floquet–Bloch theory and topology in periodically driven lattices *Phys. Rev. Lett.* **110** 200403
[6] Dal Lago V, Atala M and Foa Torres L E F 2015 Floquet topological transitions in a driven one-dimensional topological insulator *Phys. Rev.* A **92** 023624
[7] Perez-Piskunow P M, Foa Torres L E F and Usaj G 2015 Hierarchy of Floquet gaps and edge states for driven honeycomb lattices *Phys. Rev.* A **91** 043625
[8] Rodriguez-Vega M, Vogl M and Fiete G A 2021 Low-frequency and Moiré–Floquet engineering: a review *Ann. Phys., NY* **435** 168434
[9] Li J, Xu T, Zhu G-B and Pan H 2020 Photoinduced anomalous Hall and nonlinear Hall effect in borophene *Solid State Commun.* **322** 114092
[10] Vogl M, Rodriguez-Vega M and Fiete G A 2020 Effective Floquet Hamiltonians for periodically driven twisted bilayer graphene *Phys. Rev.* B **101** 235411
[11] Foa L E F, Roche S and Charlier J-C 2020 *Introduction to Graphene-Based Nanomaterials: From Electronic Structure to Quantum Transport* 2nd edn (Cambridge: Cambridge University Press)

[12] Sentef M A, Claassen M, Kemper A F, Moritz B, Oka T, Freericks J K and Devereaux T P 2015 Theory of Floquet band formation and local pseudospin textures in pump-probe photoemission of graphene *Nat. Commun.* **6** 7047
[13] D'Alessio L and Rigol M 2015 Dynamical preparation of Floquet Chern insulators *Nat. Commun.* **6** 8336
[14] Oka T and Aoki H 2009 Photovoltaic Hall effect in graphene *Phys. Rev.* B **79** 081406
[15] Calvo H L, Pastawski H M, Roche S and Foa Torres L E F 2011 Tuning laser-induced band gaps in graphene *Appl. Phys. Lett.* **98** 232103
[16] Calvo H L, Perez-Piskunow P M, Pastawski H M, Roche S and Foa Torres L E F 2013 Non-perturbative effects of laser illumination on the electrical properties of graphene nanoribbons *J. Phys.: Condens. Matter* **25** 144202
[17] Usaj G, Perez-Piskunow P M, Foa Torres L E F and Balseiro C A 2014 Irradiated graphene as a tunable Floquet topological insulator *Phys. Rev.* B **90** 115423
[18] Perez-Piskunow P M, Usaj G, Balseiro C A and Foa Torres L E F 2014 Floquet chiral edge states in graphene *Phys. Rev.* B **89** 121401
[19] Nakhaee M, Ketabi S A and Peeters F M 2018 Tight-binding model for borophene and borophane *Phys. Rev.* B **97** 125424
[20] Feng B *et al* 2017 Dirac fermions in borophene *Phys. Rev. Lett.* **118** 096401
[21] Zabolotskiy A D and Lozovik Y E 2016 Strain-induced pseudomagnetic field in the Dirac semimetal borophene *Phys. Rev.* B **94** 165403
[22] Lherbier A, Botello-Méndez A R and Charlier J-C 2016 Electronic and optical properties of pristine and oxidized borophene *2D Mater.* **3** 045006
[23] Champo A E and Naumis G G 2019 Metal-insulator transition in 8 − *Pmmn* borophene under normal incidence of electromagnetic radiation *Phys. Rev.* B **99** 035415
[24] Ibarra-Sierra V G, Sandoval-Santana J C, Kunold A and Naumis G G 2019 Dynamical band gap tuning in anisotropic tilted Dirac semimetals by intense elliptically polarized normal illumination and its application to 8 − *Pmmn* borophene *Phys. Rev.* B **100** 125302
[25] Kunold A, Sandoval-Santana J C, Ibarra-Sierra V G and Naumis G G 2020 Floquet spectrum and electronic transitions of tilted anisotropic Dirac materials under electromagnetic radiation: monodromy matrix approach *Phys. Rev.* B **102** 045134
[26] Naumis G G, Terrones M, Terrones H and Gaggero-Sager L M 2009 Design of graphene electronic devices using nanoribbons of different widths *Appl. Phys. Lett.* **95** 182104
[27] Napitu B D 2020 Photoinduced Hall effect and transport properties of irradiated 8-Pmmn borophene monolayer *J. Appl. Phys.* **127** 034303
[28] Fan X, Ma D, Fu B, Liu C-C and Yao Y 2018 Cat's-cradle-like Dirac semimetals in layer groups with multiple screw axes: application to two-dimensional borophene and borophane *Phys. Rev.* B **98** 195437
[29] Kovacic I, Rand R and Sah S M 2018 Mathieu's equation and its generalizations: overview of stability charts and their features *Appl. Mech. Rev.* **70** 020802
[30] Daniel D J 2020 Exact solutions of Mathieu's equation *Prog. Theor. Exp. Phys.* **2020** 043A01
[31] Valluri S R, Biggs R, Harper W and Wilson C 1999 The significance of the Mathieu–Hill differential equation for Newton's apsidal precession theorem *Can. J. Phys.* **77** 393–407
[32] Buchanan M 2020 The unifying role of topology *Nat. Phys.* **16** 818
[33] Lopez-Rodriguez F J and Naumis G G 2008 Analytic solution for electrons and holes in graphene under electromagnetic waves: gap appearance and nonlinear effects *Phys. Rev.* B **78** 201406(R)
[34] López-Rodríguez F J and Naumis G G 2010 Graphene under perpendicular incidence of electromagnetic waves: gaps and band structure *Phil. Mag.* **90** 2977–88
[35] Sandoval-Santana J C, Ibarra-Sierra V G, Kunold A and Naumis G G 2020 Floquet spectrum for anisotropic and tilted Dirac materials under linearly polarized light at all field intensities *J. Appl. Phys.* **127** 234301
[36] Verma S, Mawrie A and Ghosh T K 2017 Effect of electron-hole asymmetry on optical conductivity in 8 − *Pmmn* borophene *Phys. Rev.* B **96** 155418
[37] Herrera S A and Naumis G G 2019 Kubo conductivity for anisotropic tilted Dirac semimetals and its application to 8 − *Pmmn* borophene: role of frequency, temperature and scattering limits *Phys. Rev.* B **100** 195420
[38] Kibis O V 2010 Metal-insulator transition in graphene induced by circularly polarized photons *Phys. Rev.* B **81** 165433
[39] Magnus W and Winkler S 2013 *Hill's Equation* Courier Corporation (New York: Dover publications)
[40] Mojarro M A, Ibarra-Sierra V G, Sandoval-Santana J C, Carrillo-Bastos R and Naumis G G 2020 Dynamical Floquet spectrum of Kekulé-distorted graphene under normal incidence of electromagnetic radiation *Phys. Rev.* B **102** 165301
[41] Thouless D J 1983 Quantization of particle transport *Phys. Rev.* B **27** 6083–7
[42] Kristinsson K, Kibis O V, Morina S and Shelykh I A 2016 Control of electronic transport in graphene by electromagnetic dressing *Sci. Rep.* **6** 20082
[43] Lewis H R Jr 1968 Motion of a time-dependent harmonic oscillator and of a charged particle in a class of time-dependent, axially symmetric electromagnetic fields *Phys. Rev.* **172** 1313
[44] Lewis H R and Riesenfeld W B 1969 An exact quantum theory of the time-dependent harmonic oscillator and of a charged particle in a time-dependent electromagnetic field *J. Math. Phys.* **10** 1458–73
[45] Berry M V 1984 Quantal phase factors accompanying adiabatic changes *Proc. R. Soc.* A **392** 45–57
[46] Vanderbilt D 2018 *Berry Phases in Electronic Structure Theory: Electric Polarization, Orbital Magnetization and Topological Insulators* (Cambridge: Cambridge University Press)
[47] Xiao Di, Chang M-C and Niu Q 2010 Berry phase effects on electronic properties *Rev. Mod. Phys.* **82** 1959–2007
[48] Tamir T 1962 Characteristic exponents of Mathieu functions *Math. Comput.* **16** 100–6
[49] Aharonov Y and Anandan J 1987 Phase change during a cyclic quantum evolution *Phys. Rev. Lett.* **58** 1593–6
[50] Page D N 1987 Geometrical description of Berry's phase *Phys. Rev.* A **36** 3479–81
[51] Moore D J 1991 The calculation of nonadiabatic Berry phases *Phys. Rep.* **210** 1–43
[52] Moore D J and Stedman G E 1990 Non-adiabatic Berry phase for periodic Hamiltonians *J. Phys. A: Math. Gen.* **23** 2049